Supplementary information

A self-adsorption molecule passivated interface enables efficient and stable lithium metal batteries

Gongxun Lu[1#], Xinru Wu[1#], Miaofei Huang[1#], Mengtian Zhang[1], Zhihong Piao[1], Xiongwei Zhong[2], Chuang Li[1], Yanze Song[1], Chengshuai Chang[1], Kuang Yu[1], Guangmin Zhou[1]*

1 Tsinghua-Berkeley Shenzhen Institute & Tsinghua Shenzhen International Graduate School, Tsinghua University, Shenzhen 518055, P. R. China.

2 Department of Materials Science and Engineering, Southern University of Science and Technology, Shenzhen 518055, China.

* Corresponding author: guangminzhou@sz.tsinghua.edu.cn

Method

Experimental section

Materials

LiFSI (DoDo chem) and HFA (Macklin, 98%) were directly used as received. DME (Dodo chem), TTE (1,1,2,2-tetrafluoroethyl 2,2,3,3-tetrafluoropropylether) (Macklin), were purified by 300 ℃ pretreated molecular sieves (Aladdin) before use. A conventional carbonate electrolyte 1 M $LiPF_6$ in EC: ethyl methyl carbonate (1:1 v/v) + 5% fluoroethylene carbonate (DoDo chem) is used as received as the baseline electrolyte. 1.5 M LiFSI in DME is used as a baseline electrolyte. 1 wt% HFA is added in LiFSI/DME for the experimental electrolyte. The electrolytes were prepared in an argon-filled glovebox and stirred overnight. NCM811 laminates (mass loading ~ 8 mg cm^{-2} to 20 mg cm^{-2}), LCO laminates, 50 μm lithium foil and 400 μm lithium foil, Cu foil, Al foil, and 2032-type coin cell cases were provided by Guangdong Canrd New Energy Technology Co. Ltd. Dry 1-Ah NCM811||Li pouch cells were obtained from Guangdong Canrd New Energy Technology Co. Ltd.

Cell assembly and electrochemical measurements

2032-type coin cells were assembled with one layer of Celgard 2500 as the separator for all electrochemical characterizations. 40 μL electrolyte is injected into all coin cells. All cells were assembled in an argon-filled glovebox. LSV, CV, and EIS were tested on Biologic SP150 and CHI 760D electrochemical workstations. LSV and CV curves were tested in Li||Al and Li||Cu asymmetric cells at scan rates of 2 mV s^{-1} and 5 mV s^{-1}, respectively. EIS was tested using Li||Li cells with 10 mV amplitude and frequency ranging from 100 mHz to 1 MHz. t_{Li^+} was measured by applying a polarization voltage of 10 mV to Li||Li cells for 2 h, and resistances before and after polarization were measured by EIS. For Li-Cu cell CE cycling tests, five pre-cycles between 0.01 and 1.5 V were initialized to minimize the side reaction between the Li and Cu electrode surface, and then cycling was done by depositing Li onto the Cu electrode; the Li was then stripped to 1.5 V at different current densities. For the Aurbach's CE test, a standard protocol was followed: Coulombic efficiency = $(nQc + Q_R)/ (nQc + Q_T)$. Q_T indicated an initial total Li plating capacity of 5 mAh cm^{-2}, Qc indicated a fixed cycling capacity of 1 mAh cm^{-2}, and Q_R indicated capacity retention measured by a final Li stripping process. In situ EIS using NCM811||Li with 10 mV amplitude and frequency ranging from 10 mHz to 1 MHz was tested by measuring every 0.1 V increase/decrease in voltage during cycling at a current density of 0.1

C. DRT analyze was conducted by tools developed by Ciucci's group[1]. Multichannel battery testers (LAND, Wuhan China, and Neware, Shenzhen China) were used for galvanostatic charge/discharge tests at different current densities. An additional Al foil and Al-clad cathode lids (Shenzhen Kejing Star Technology Co.) are used when assembling NCM811||Li cells to prevent electrolyte corrosion on stainless steel during the test. LMA and cathodes for further characterization were collected from NCM811||Li cells that cycled at 0.5 C at 4.5 V for 50 cycles and washed with the solvent.

Material characterizations

^{19}F NMR was performed on a Bruker Avance Ill HD600 MHz at room temperature using $CDCl_3$ as a solvent. Raman spectra were collected on a HORIBA HR Evolution with a 785 nm laser source. The chemical composition of SEI and CEI is analyzed by XPS (PHI 5000 VersaProbe II, Escalab Xi+). The spatial distribution information of CEI and SEI components was collected by time-of-flight secondary ion mass spectrometry (ToF-SIMS, PHI Nano ToF2), with a sputter rate of 0.3nm s^{-1} (Ar^+) for SiO_2, 3 keV, 100 nA, 50*50 μm. The morphology and microstructure were observed by SEM (HITACHI SU8010). To measure TM dissolution, cycled LMA is dissolved in 10 ml deionized H_2O, and the Ni/Co/Mn element content in the solution was tested using Arcos II MV. XRD was performed by Rigaku MiniFlex 600 with filtered Cu Kα radiation (λ = 1.5405 Å). FTIR spectra were collected on an infrared spectrophotometer (Nicolet 6700). TEM characterizations were performed on transmission electron microscopy (Talos F200X G2, 200 kV) operated at 200 kV. For sample preparation, the copper mesh was placed on the copper electrode side of the Li-Cu cell and removed after 10 cycles. After removing excess lithium salts with DME solvent, the sample was transferred to the TEM for observation. The detailed sample preparation process is shown in Fig. S32. The thermal stability of CEI formed in different electrolytes was measured by differential scanning calorimetry (DSC, Mettler Toledo DSC 3) at a scan rate of 5 °C min^{-1} between 25 and 350 °C.

DFT simulation

In this work, density functional theory (DFT)[2] was employed to study molecules' HOMO and LUMO. The structural optimization of all structures was performed using the B3LYP[3] level of DFT with the 6-311g+(d,p) basis sets[4, 5]. All the calculations were carried out using the Gaussian 09 package.

First-principle calculations

First-principle calculations were performed using the Vienna ab initio simulation package (VASP) [6]. Core electrons are described using the projector-augmented-wave method [7] with

the standard Perdew-Burke-Ernzerhof [8] of generalized gradient approximation [9], as exchange-correlation functional. The plane-waves of kinetic energy were set at 400 eV. The first Brillouin zone of slab calculations was sampled using a Γ-centered k-point grid of 3 × 3 × 1 for geometry optimization. For the adsorption model, a supercell of NCM (001) surface keeping the seven bottom layers fixed to describe the bulk properties and 20 Å vacuum layers were selected for simulation. The dissociation energy (E_dis.) between NCM slab and different molecules was defined as follows. All models are displayed by software VESTA[10].

E_dis=E_(NCM-slab+molecules_F)− E_(NCM-slab+molecules)

where E_(NCM-slab+molecules) and E_(NCM-slab+molecules_F) are the total energy of the adsorption configurations of molecules with and without C-F, E_molecules is the energy of adsorbates and E_(NCM-slab) is the energy of the NCM (001).

MD simulations

The electrolyte systems were initially configured using the PACKMOL package[6], with species randomly placed in a 5 × 5 × 5 nm^3 cubic box. The OPLS-AA force field[7] was used for Li^+, DME and HFA, while the force field parameters for FSI^- were obtained directly from the literature[8]. The restrained electrostatic potential charges (RESP) was applied to further secure the accuracy of non-bonded interactions. MD simulations were performed using the GROMACS[9] software version 2019.5.

The prepared systems were first minimized using the conjugated gradient with a convergence criterion of 100 kcal mol^{-1} Å. For equilibration of the system, firstly, the systems were equilibrated to a temperature of 298 K and a pressure of 1 atm in the NPT ensemble for 2 ns. Then the systems were heated from 298 K to 500 K for 1 ns, and maintained at 500 K for 2 ns, and annealed from 500 K to 298 K in 1 ns, followed by maintaining at 298 K for 2ns at 1 atm. The Velocity-rescale temperature coupling[10] and the Berendsen pressure coupling were employed to control the temperature and the pressure. Finally, production runs of 15 ns were carried out at 298 K and 1 atm using the Velocity-rescale temperature coupling and the Parrinello-Rahman pressure coupling. Only the last 10 ns were sampled to assess the radial distribution function (RDF) and coordination structure counting, with the trajectory saved for each 10 ps. The van der Waals interactions and short-range Coulomb interactions were truncated at a cutoff distance of 1.2 nm and the Particle-mesh Ewald (PME) method was used for long-

range electrostatic interactions throughout. All MD simulations were carried out with three-dimensional periodic boundary conditions using the leap-frog integrator with a time step of 0.001 ps.

Moreover, the equilibrated electrolyte systems were added between two graphene slabs to simulate the electrode-electrolyte interface. The force field parameters of graphene slabs were transferred from the default OPLS-AA force field in GROMACS. As our research focuses on the changes of interfacial structure caused by HFA, only zero charge potential was considered for the two systems. The constant charge method has been found appropriate for modeling the behavior of open electrode system at the equilibrium state[11]. A layer of vacuum of 10 nm was wadded in the z-direction to separate periodic images and reduce Columbic interactions between the mirrored slabs. Following that, an NPT equilibration was performed for 2 ns using the Velocity-rescale temperature coupling and the Berendsen pressure coupling. During the NPT simulation, the size of x and y axis were fixed to make sure the box size can fit the lattice constant of the graphene slab. Then, an NVT production run at 298.15 K for 40 ns, from which number density profiles were extracted and analyzed.

The further statistics were analyzed from the simulated trajectory data using the Gromacs tool-suites, the Visual Molecular Dynamic (VMD) program[12] and some python scripts written by ourselves.

FEM simulation method

We performed the finite element analysis based on the Comsol Multiphysics 6.2 platform. The core simulation strategy emulates how electrolyte solvent (DME) reacts with the cathode to form a CEI layer, where HFA-containing electrolytes mitigate such side reaction. The presence of HFA-containing electrolytes is deemed to suppress this side reaction effectively, resulting in the formation of thin and uniform CEI layer that is enriched with inorganic constituents, which exhibit higher conductivity compared to that without HFA. Concurrently, the depletion of DME leads to reduced electrolyte transport within the cathode, further lowering the battery's performance.

The entire simulation consists of two major steps. First, a one-dimensional numerical simulation model is employed to establish the relationship between the morphology evolution of the CEI and the battery cycling process, as well as to simulate the changes in the internal environment of the battery, such as CEI impedance, and electrolyte consumption. Subsequently,

the integrated parameters representing different cycle stages obtained from this numerical simulation model are incorporated into a three-dimensional model, thereby yielding a visualization of the internal physical fields. The following are the main simulated equations:

In the cathode, apart from the primary lithium-ion intercalation reaction, we also take into account the side reactions involving solvent molecules and the formation of a CEI on the cathode surface:

$$S + nLi^+ + ne^- \rightarrow P_{CEI}$$

where, S represents the solvent, and P_{SEI} denotes the products formed during the reaction, and n is the number of lithium ions consumed. The generation of P_{SEI} leads to the loss of lithium inventory within the battery, causing an increase in the resistance of the CEI, as well as a decrease in the electrolyte volume fraction within the cathode.

The kinetics of this side reaction can be expressed by:

$$i_{loc,CEI} = -(1 + \mathrm{HK})\frac{i_{loc}}{\exp\left(\frac{\alpha_a F\eta}{RT}\right) + \frac{q_{CEI} fJ}{i_{loc}}}$$

where i_{loc} is the local current density as mentioned above, HK is a dimensionless number representing the cathode expansion factor, which depends on the cathode's state of charge. HK is zero during the lithiation process. J is a dimensionless number representing the exchange current density for parasitic reactions. q_{CEI} signifies the local cumulative charge caused by the formation of the CEI. f =is a lumped dimensionless parameter based on the properties of the CEI film.

The concentration c_{CEI} of CEI can be used to calculate the CEI thickness as follows:

$$\frac{\partial c_{CEI}}{\partial t} = -\frac{\gamma_{CEI} i_{loc,CEI}}{nF}$$

where γ_{CEI} is the stoichiometric coefficient of CEI.

The q_{CEI} above is directly proportional to the c_{CEI}:

$$q_{SEI} = -\frac{F c_{SEI}}{A_v}$$

where A_v is area of electrode surface.

Then the thickness of SEI layer δ_{CEI} can be calculated:

$$\delta_{CEI} = -\frac{M_P c_{CEI}}{A_v \rho_P}$$

where M_P and ρ_P is the molar mass and density of CEI, respectively.

The following are the governing equations for the fundamental electrochemical reactions:

In the electrolyte, the transport of ions is governed by the Nernst−Planck equation:

$$N_i = -D_{e,i}\left(\nabla c_{e,i} - \frac{z_i F c_{e,i}}{RT}\nabla \Phi\right)$$

where N_i is flux, $D_{e,i}$, z_i and $c_{e,i}$ is the diffusion coefficient in the electrolyte, charge and concentration of species i, respectively. F is the Faraday's constant, R is the ideal gas constant, T is the Kelvin temperature and Φ is the electrolyte potential.

The ions present within the electrolyte adhere to the principles of both mass conservation and charge conservation, which can be represented as:

$$\frac{\partial c_{e,i}}{\partial t} + \nabla \times N_i = 0$$

$$\sum_i z_i\, c_{e,i} = 0$$

where z_i is the valence of each species in the electrolyte.

At the interface of electrolyte and the electrode, the electron transfer between Li^+ and Li atoms can be expressed by the following simplified reaction:

$$Li^+ + e^- \leftrightarrow Li$$

This reaction could be quantified by the Butler-Volmer equation:

$$i_{loc} = i_{ex}\left[\exp\left(\frac{\alpha_a F\eta}{RT}\right) - \exp\left(\frac{-\alpha_c F\eta}{RT}\right)\right]$$

where i_{loc} is the local current density, which could be used to quantify the local reaction rate. η is overpotential, α_a and α_c are the anodic and cathodic charge transfer coefficients, respectively, and i_{ex} is exchange current density.

The overpotential can be calculated as:

$$\eta = \phi_s - \phi_e - U_{eq}$$

where ϕ_s and ϕ_l is the solid phase and liquid phase potential, respectively, U_{eq} is the equilibrium potential of the reaction.

In the cathode/anode particles, Li atoms diffuse into/out the inner/outer particles due to the concentration gradient, and could be expressed by the Fick's second law:

$$\frac{\partial c_s}{\partial t} = D_s\left(\frac{\partial^2 c_s}{\partial r^2} + \frac{2}{r}\frac{\partial c_s}{\partial r}\right)$$

where D_s is the diffusion coefficient of Li atoms in the cathode particles, r is the radius of

particle, c_s is the Li atom concentration.

The open-circuit potential U of cathode can be calculated according to the Nernst equation:

$$U = U_{eq} + \frac{RT}{nF} ln\left(\frac{c_{e,Li}}{c_s}\right)$$

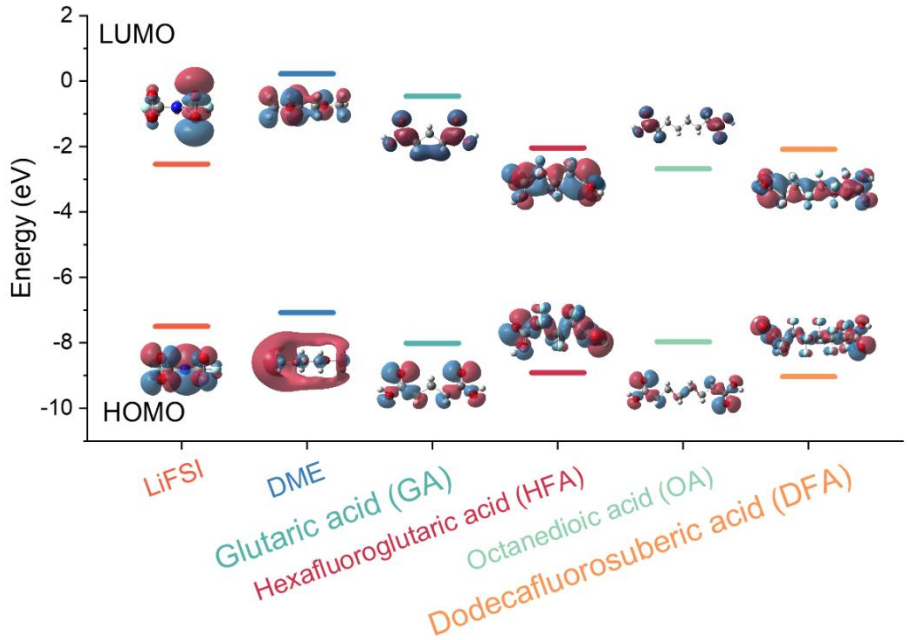

Figure S1 HOMO/LUMO energy levels of LiFSI, DME and various additives molecules.

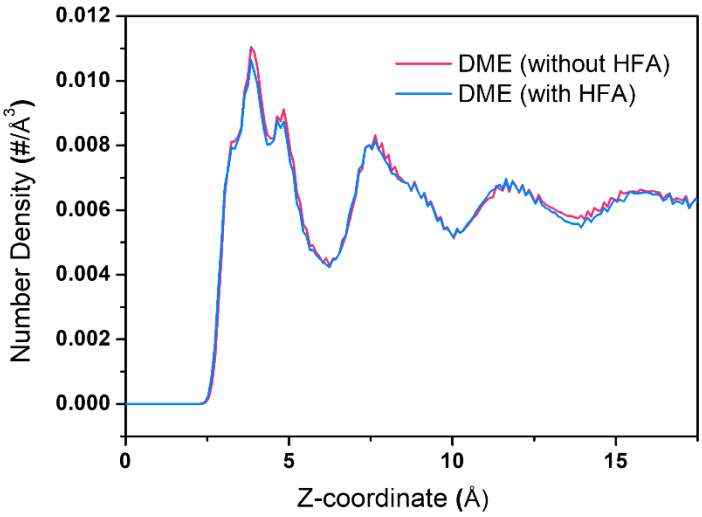

Figure S2 The number densities of DME solvent molecules in the inner Helmholtz layer via MD simulation.

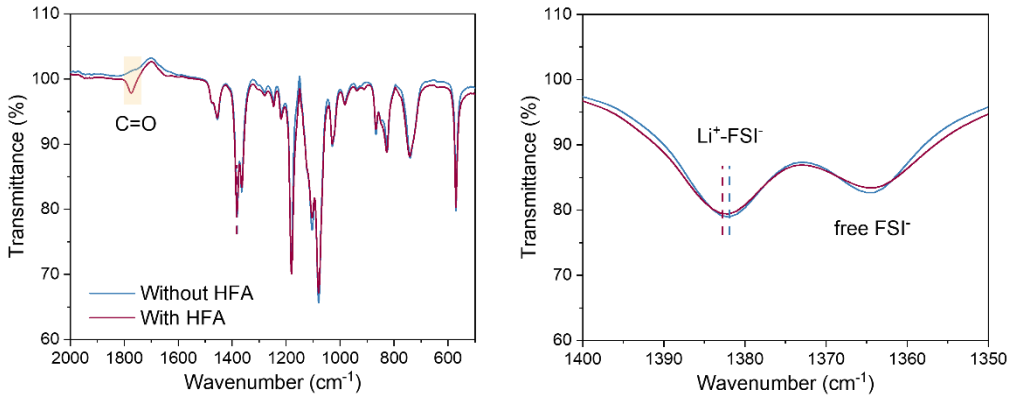

Figure S3 FTIR spectra of LiFSI/DME with/without HFA addition.

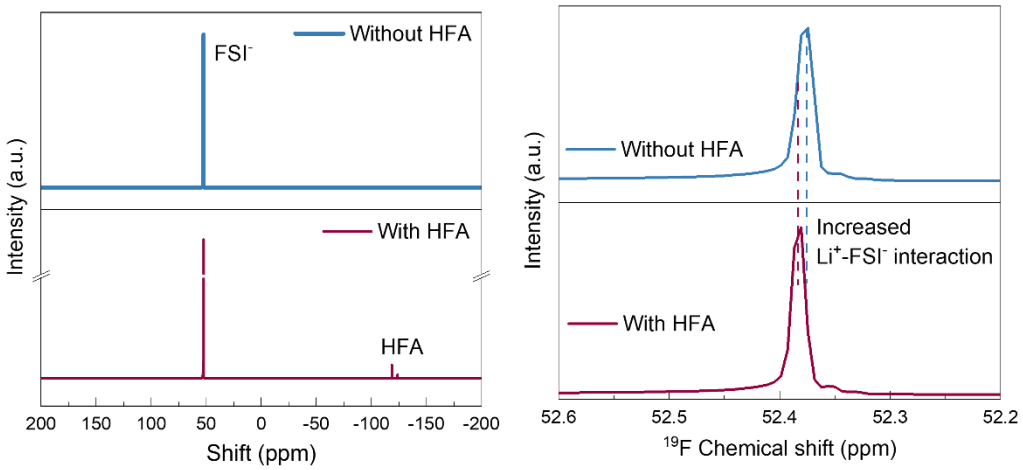

Figure S4 ^{19}F NMR of LiFSI/DME with/without HFA.

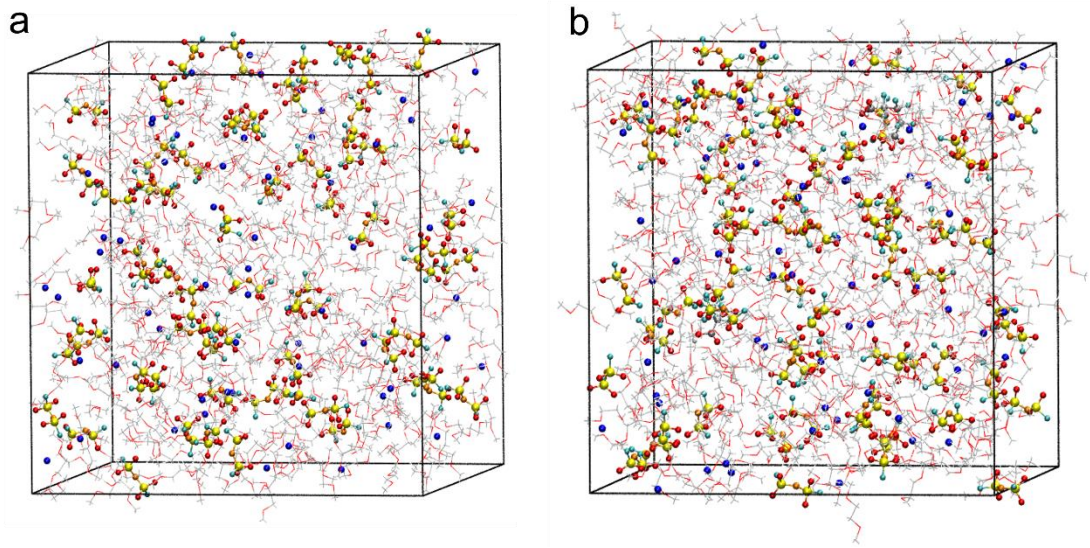

Figure S5 Snapshot of the simulation box of (a) LiFSI/DME and (b) LiFSI/DME+HFA.

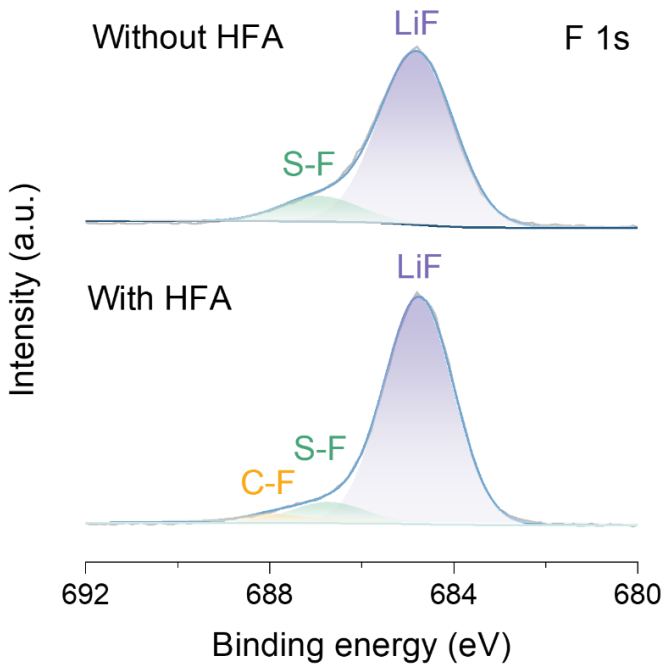

Figure S6 The F 1s spectra of CEI on NCM811 cycled in electrolyte with or without HFA.

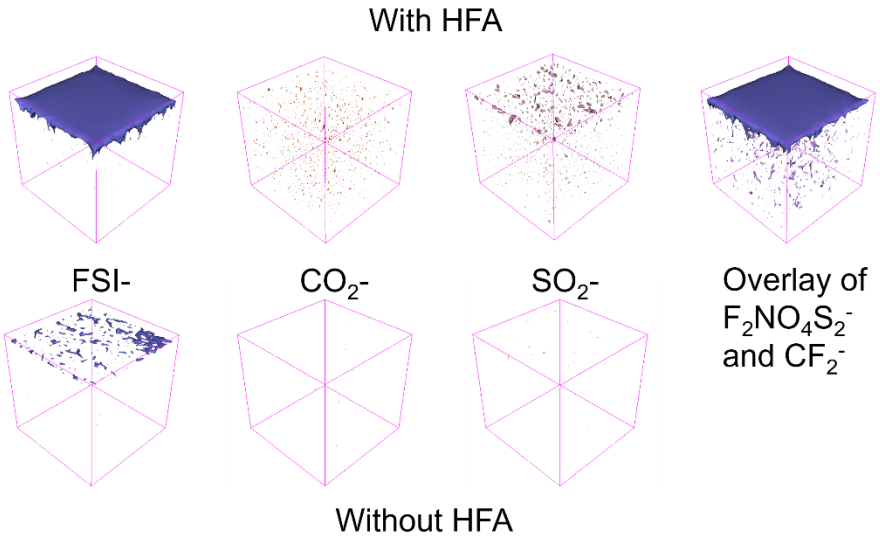

Figure S7 3D views of CO_2^-, SO_2^-, $F_2NO_4S_2^-$ distribution in CEI on NCM811 cycled in electrolyte with or without HFA addition.

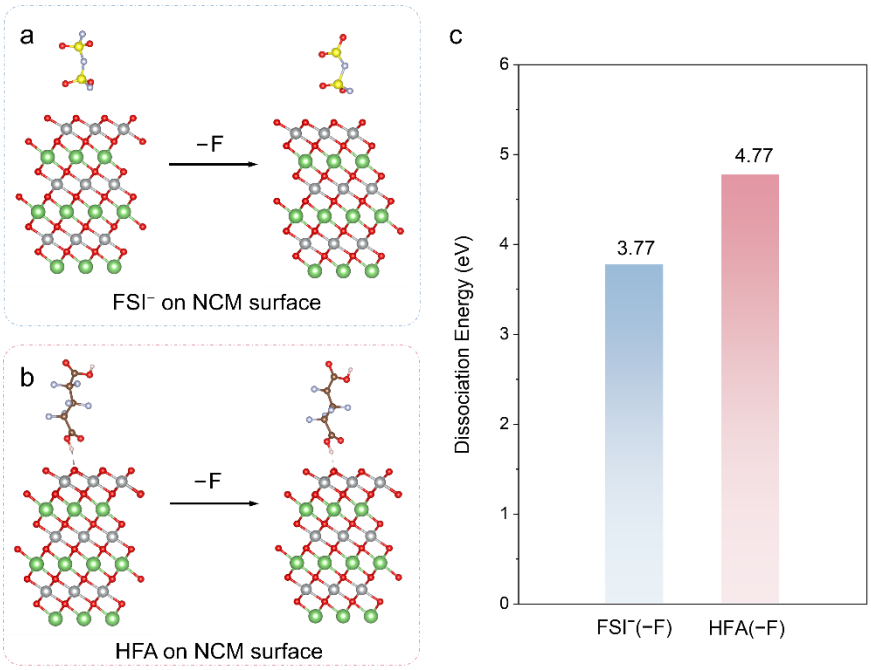

Figure S8 The defluorination process (a,b) and calculated dissociation energy (c) of FSI^- and HFA molecules on NCM surface.

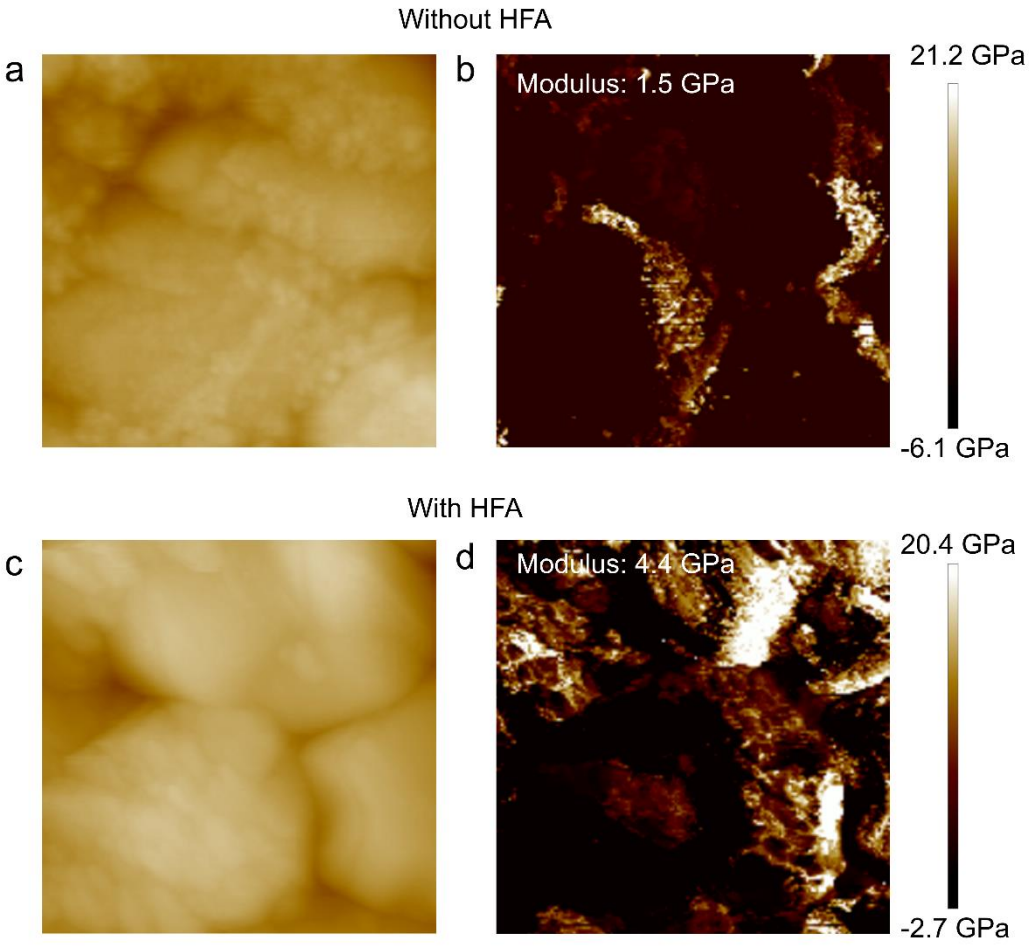

Figure S9 Atomic force microscopy topography image (a) and the distribution of Young's modulus (b) of the CEI on NCM811 cycled without HFA. Atomic force microscopy topography image (c) and the distribution of Young's modulus (d) of the CEI on NCM811 cycled with HFA addition.

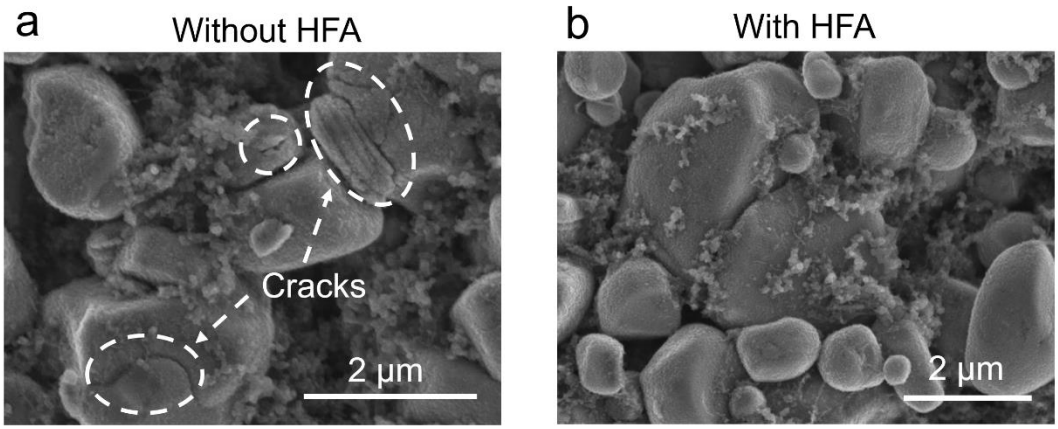

Figure S10 SEI images of the cycled NCM811 using the electrolytes (a) without and (b) with HFA, respectively.

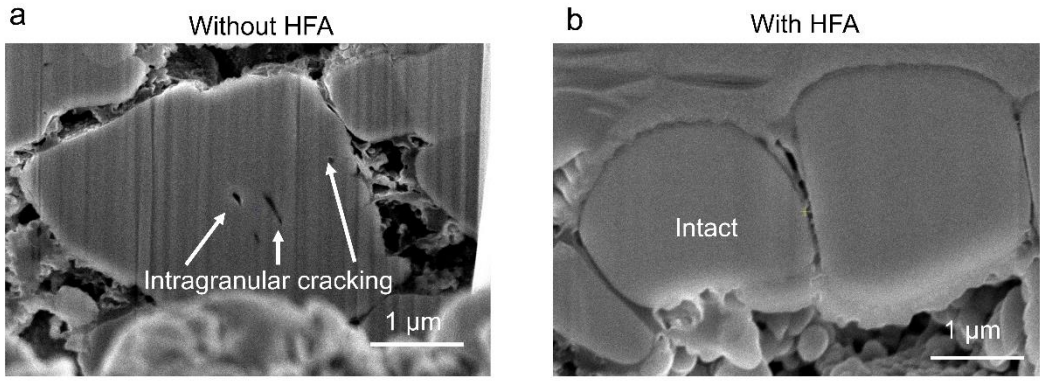

Figure S11 FIB-SEM images of the cycled NCM811 using the electrolytes without and with HFA, respectively.

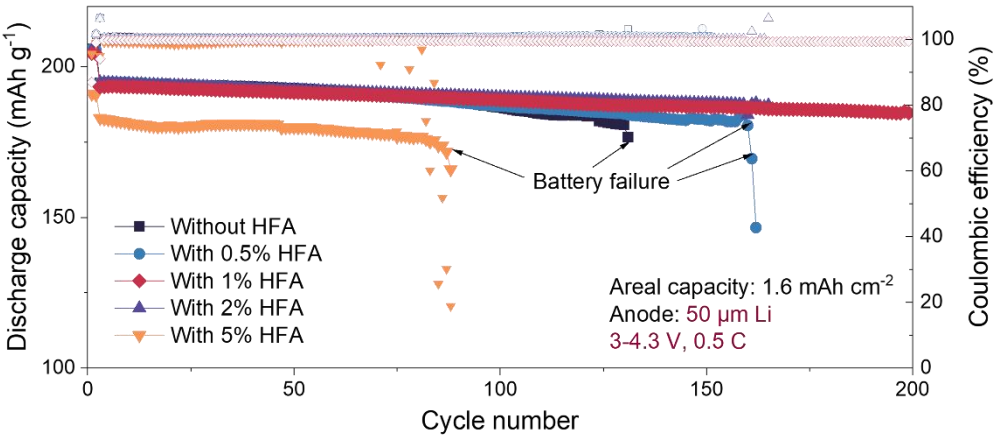

Figure S12 Cycling performance of NCM811||Li cells using electrolytes with HFA addition at different concentrations.

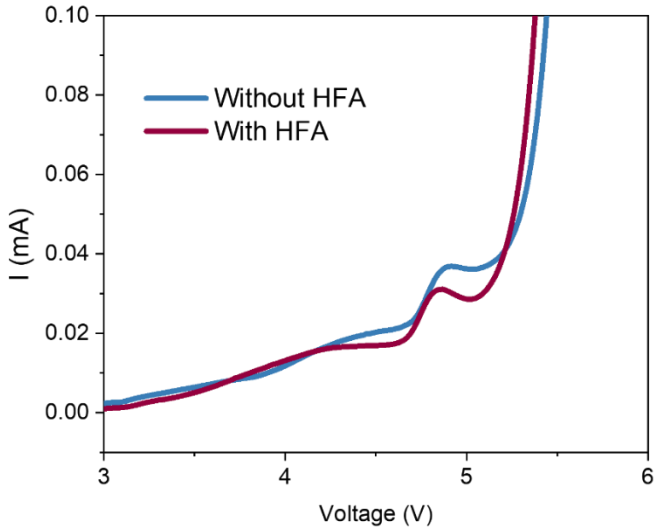

Figure S13 Oxidative stability measured via LSV for Li||Al cells.

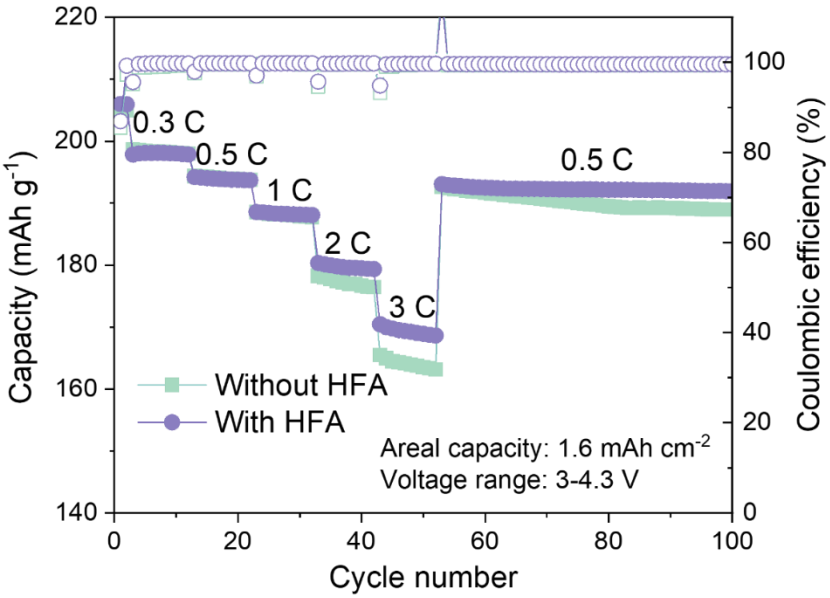

Figure S14 Rate capability of NMC811||Li cells under different charging/discharging rates at voltage range of 3-4.3 V.

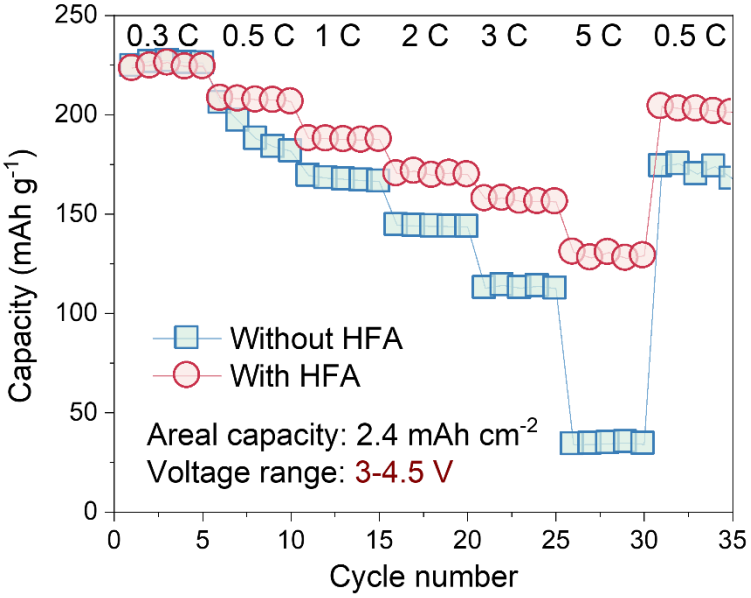

Figure S15 Rate capability of NMC811||Li cells under different charging/discharging rates at voltage range of 3-4.5 V.

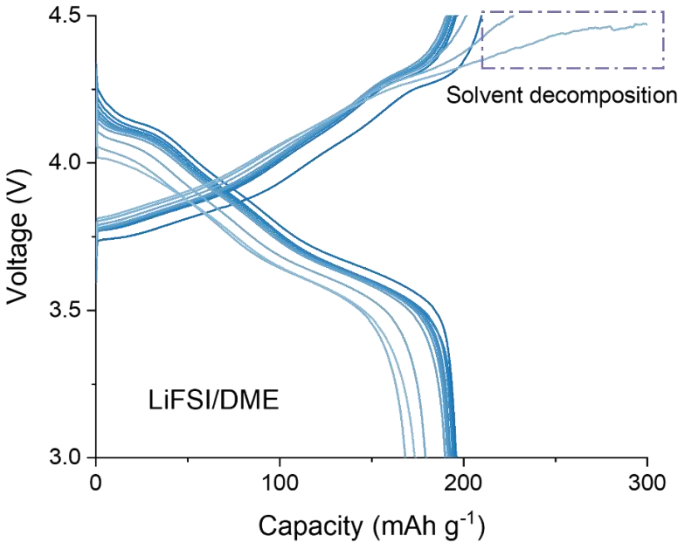

Figure S16 The voltage capacity curve of NCM811||Li using electrolytes without HFA at voltage range of 3-4.5 V.

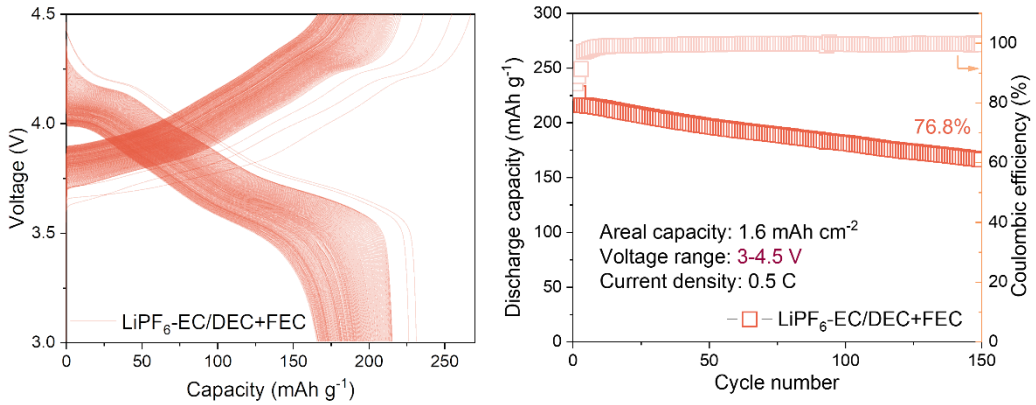

Figure S17 The voltage capacity curve and cycling performance of NCM811||Li cells using electrolytes of $LiPF_6$-EC/DEC+FEC at voltage range of 3-4.5 V.

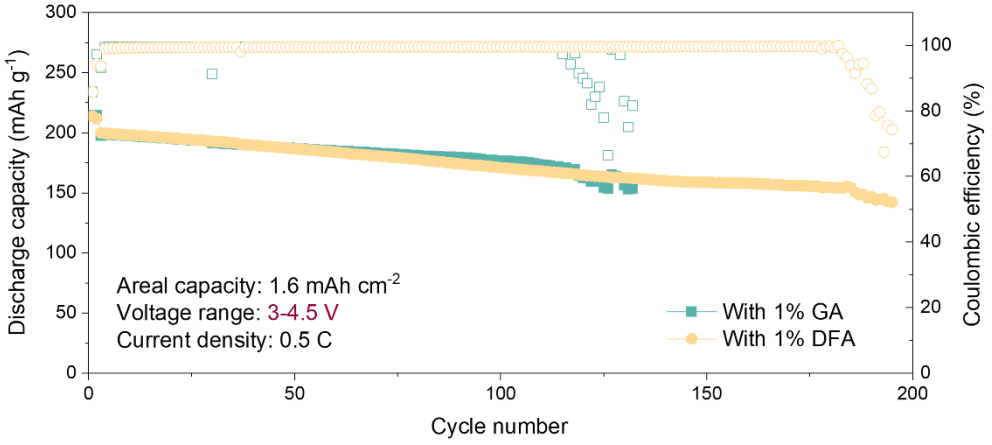

Figure S18 Cycling performance of NCM811||Li cells using electrolytes with GA and DFA addition.

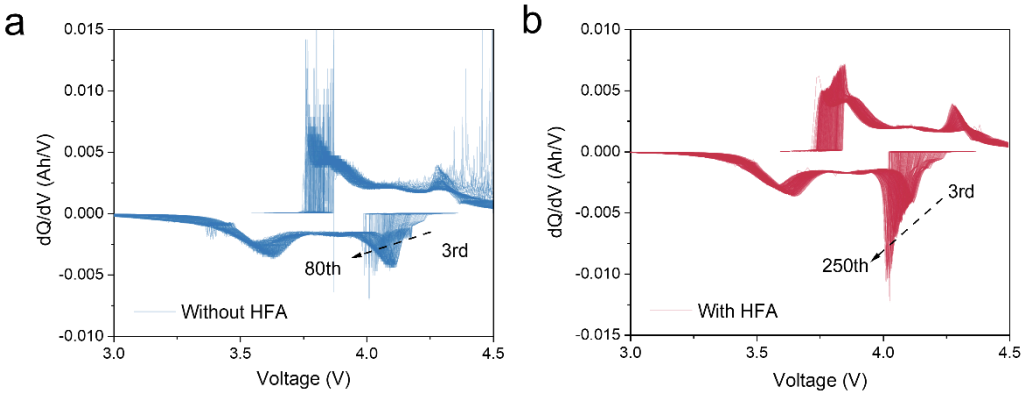

Figure S19. dQ/dV curves of NCM811||Li cells using electrolytes of without (a) and with HFA (b) at voltage range of 3-4.5 V

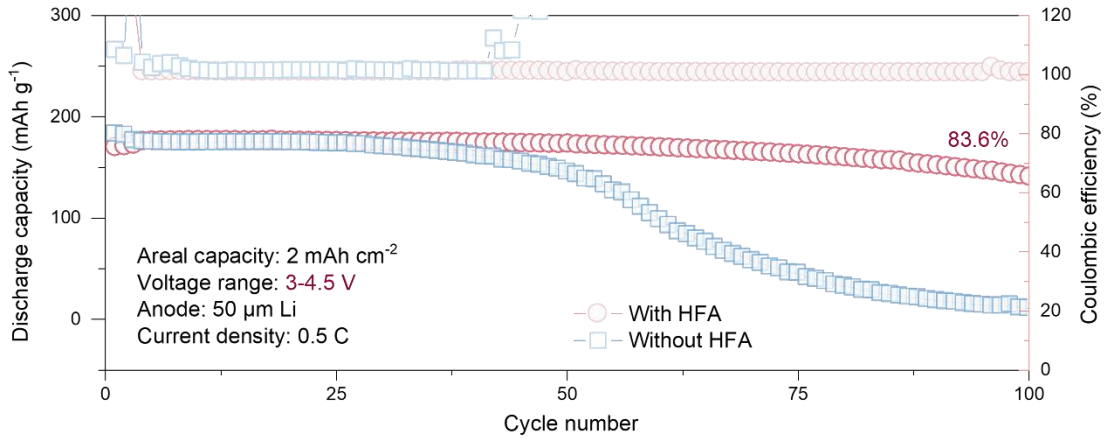

Figure S20 Cycling performance of LCO||Li cells using electrolytes with or without HFA addition.

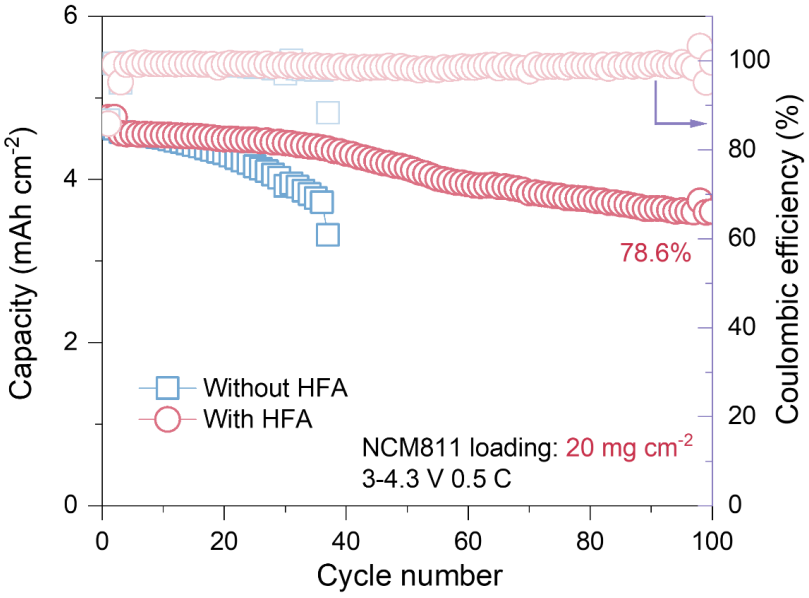

Figure S21 Cycling performance of NCM811||Li cells using electrolytes with/without HFA.

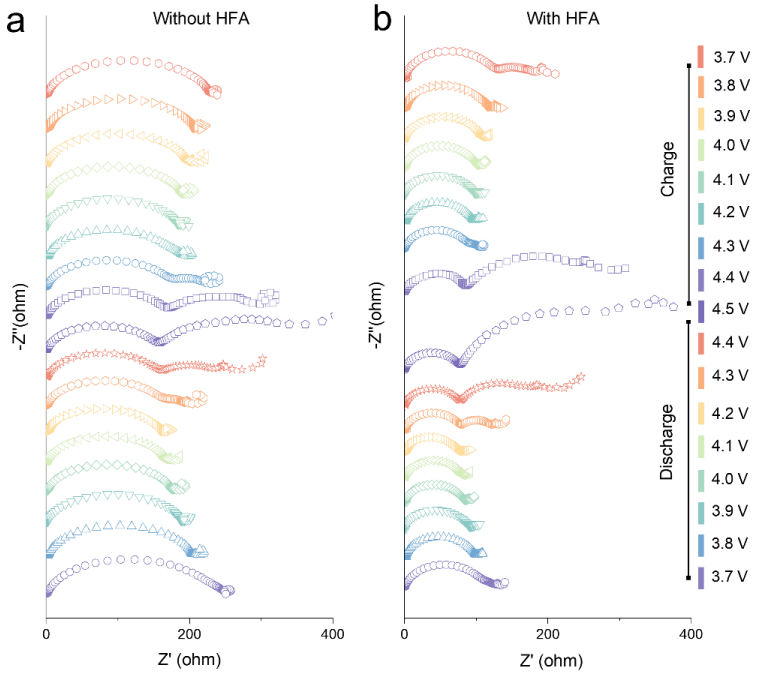

Figure S22 In-situ EIS of cycled NCM811||Li cells with different electrolytes during charge/discharge at a cut-off voltage of 4.5 V.

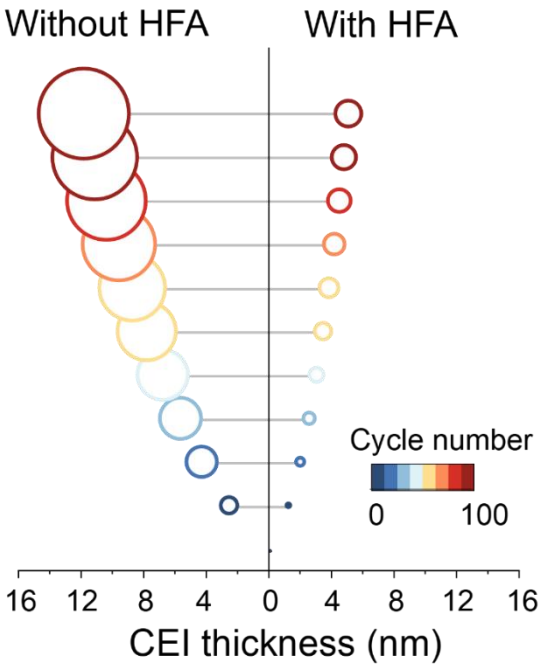

Figure S23 Comparison of FEM simulated CEI thickness evolution during cycling under electrolyte with or without HFA.

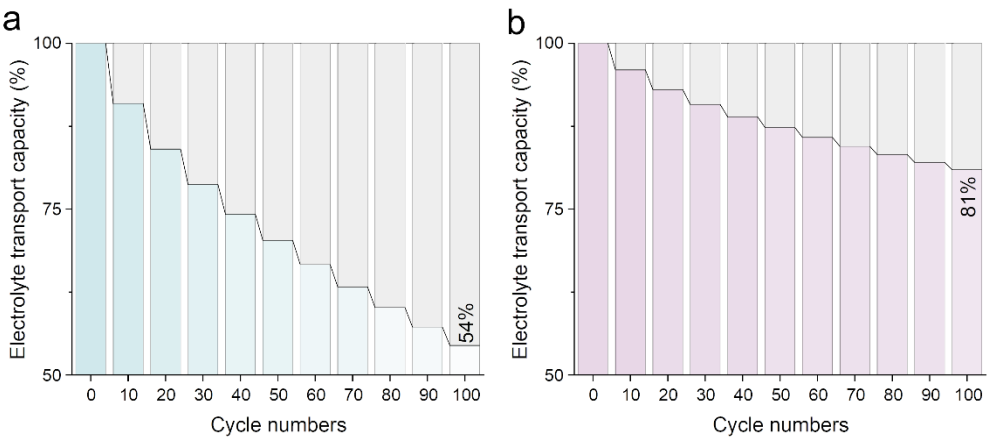

Figure S24 FEM simulation results of the electrolyte transport capacity evolution in (a) without HFA (b) with HFA during cycling due to the reaction between DME and cathode.

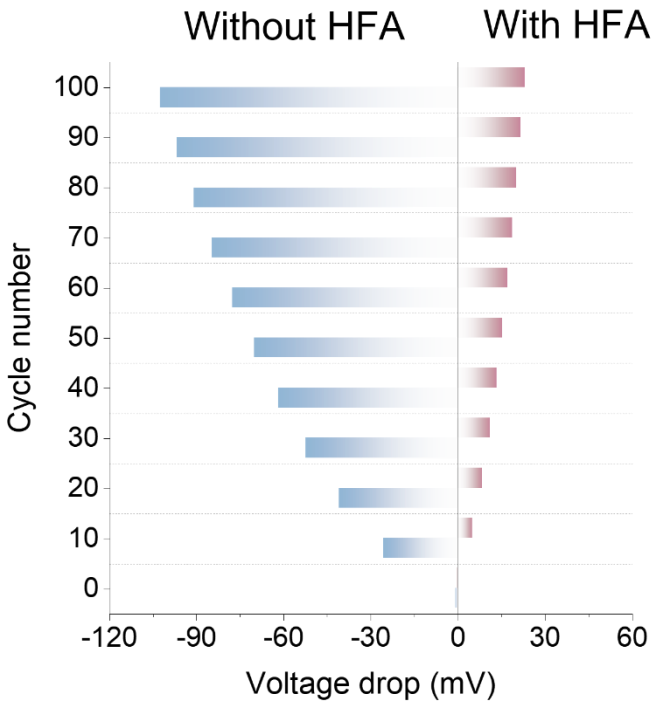

Figure S25 FEM simulation results of the voltage drop due to different thicknesses and electrical conductivities of two CEI.

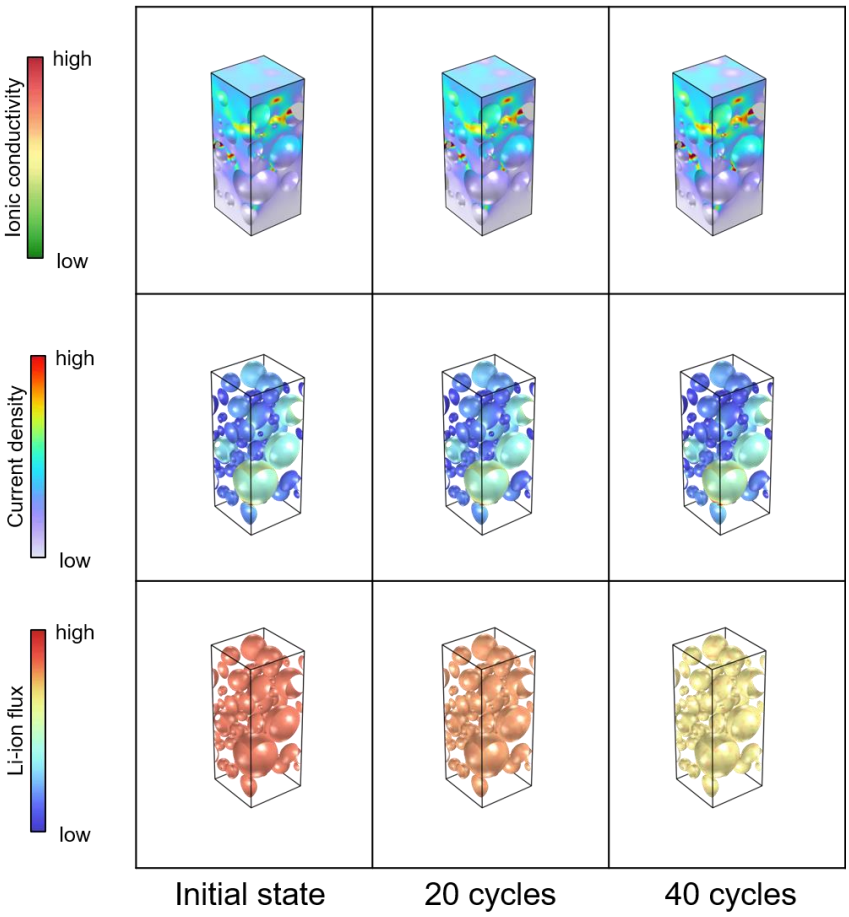

Figure S26 FEM simulation results of the physical field (e.g., ionic conductivity of CEI, current density in the electrolyte and Li-ion flux at the cathode surface) distributions within the internal cathode structure of baseline electrolyte during cycling.

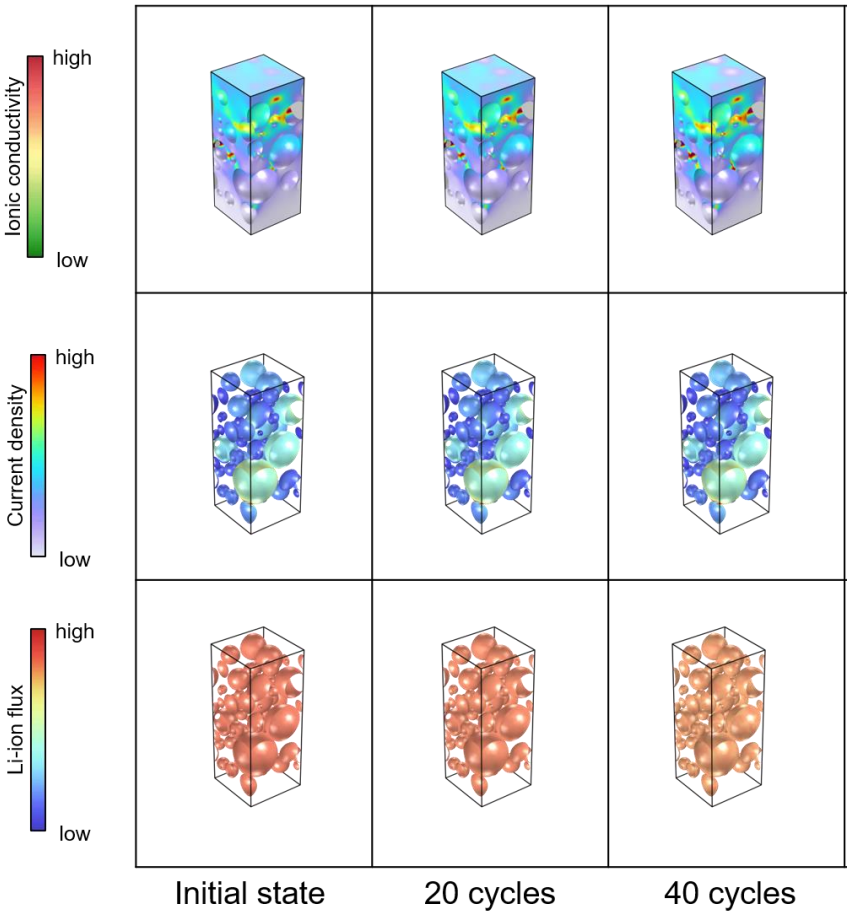

Figure S27 FEM simulation results of the physical field (e.g., ionic conductivity of CEI, current density in the electrolyte and Li-ion flux at the cathode surface) distributions within the internal cathode structure of electrolyte with HFA during cycling.

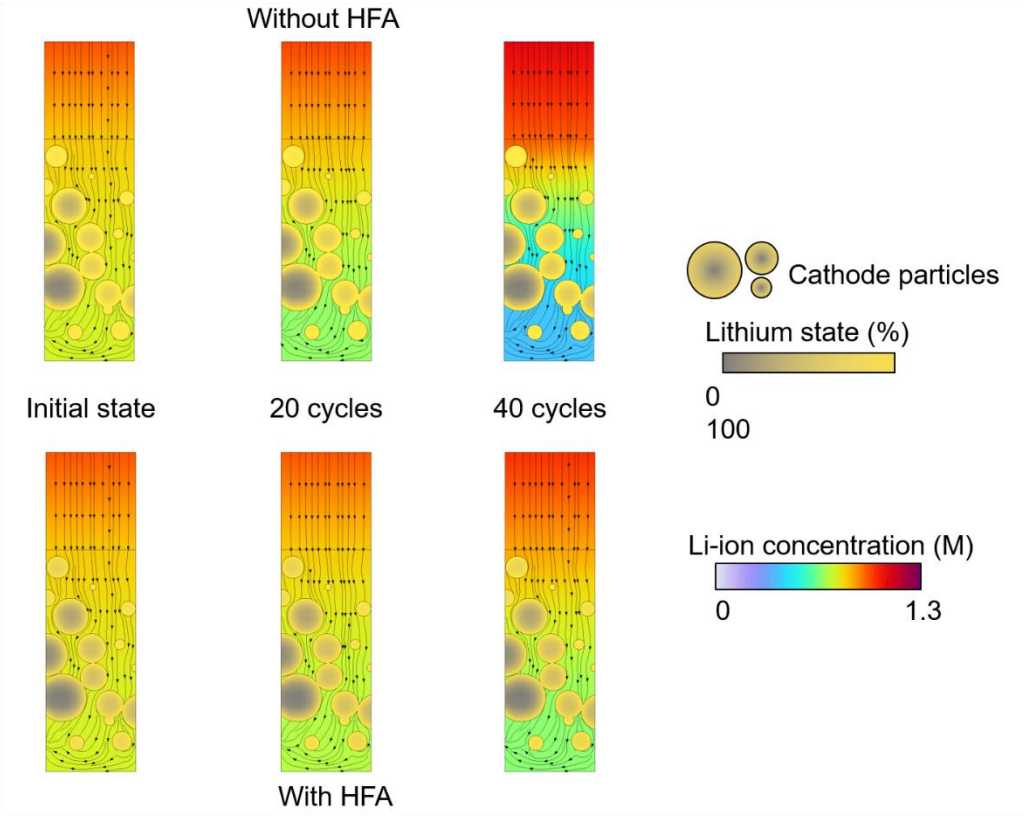

Figure S28 Simulated evolution of lithium-ion concentration and lithiation state within cathode at the 100% depth of discharge under different cycles for different electrolytes.

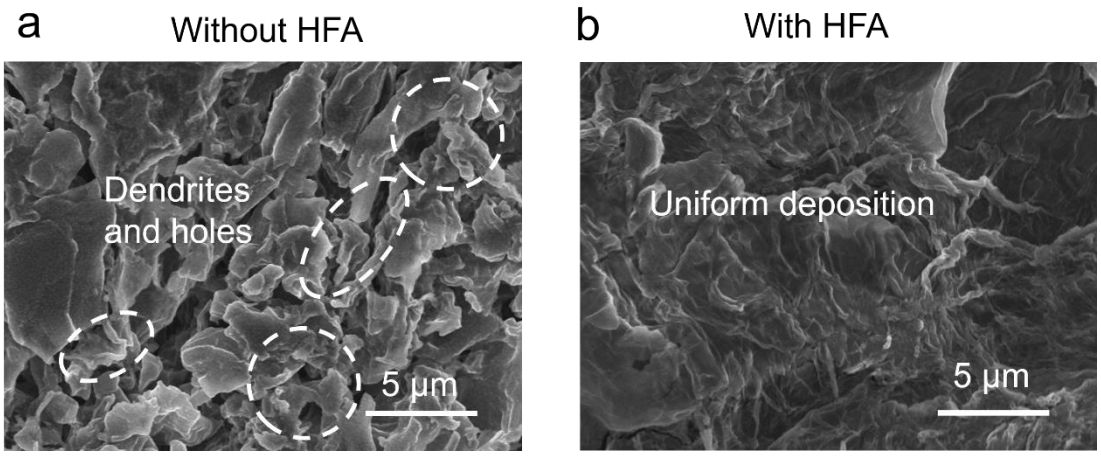

Figure S29 The SEM images of Li deposition morphology of different electrolytes after 50 cycles.

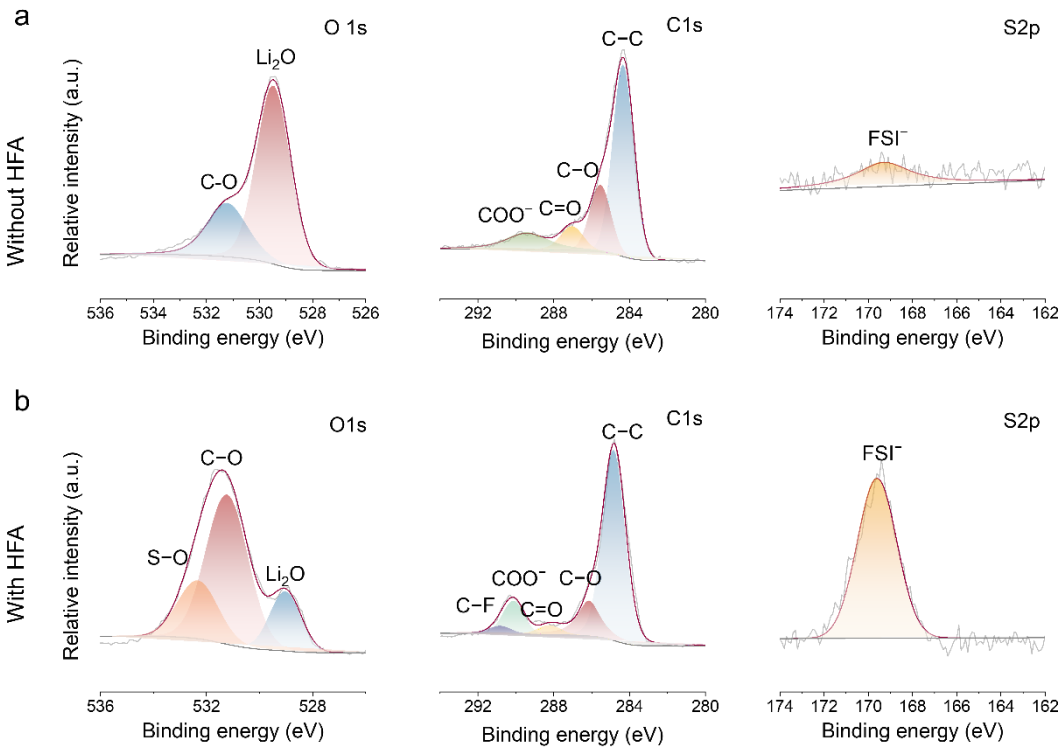

Figure S30 The XPS spectrum of SEI on lithium metal surface after 30 cycles in electrolyte without HFA (a) and with HFA (b).

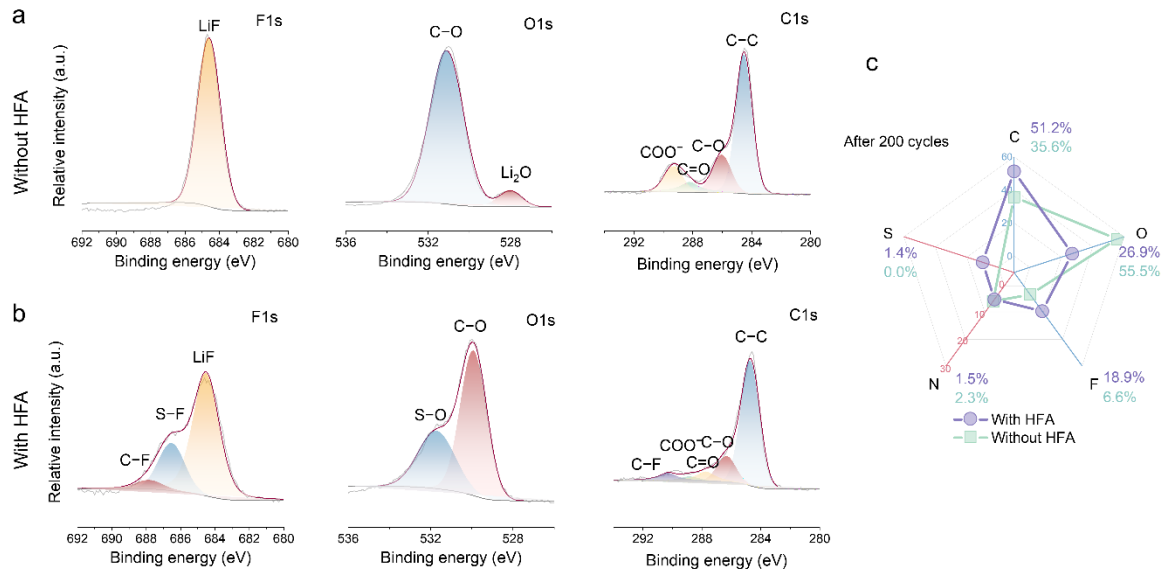

Figure S31 The XPS spectrum of SEI on lithium metal surface after 200 cycles in electrolyte of without HFA (a) and with HFA (b). **c** Atomic ratio derived from XPS spectra of SEI on lithium metal surface after 200 cycles in different electrolytes.

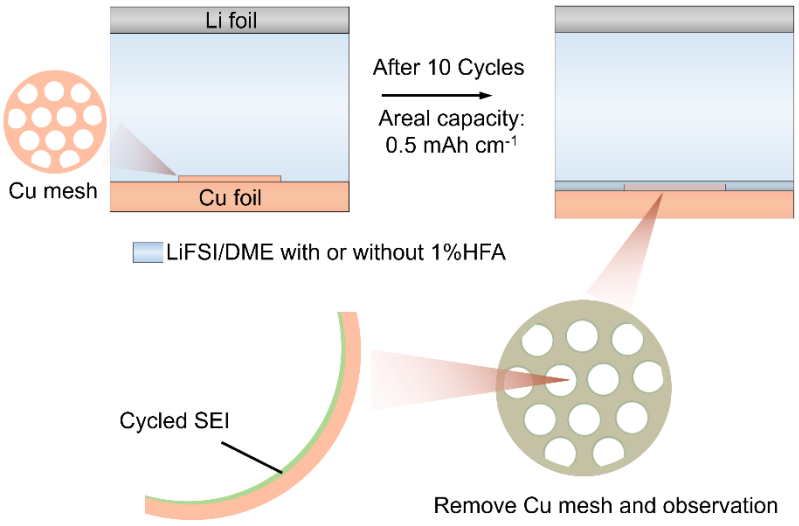

Figure S32 The detailed sample preparation process for TEM characterization.

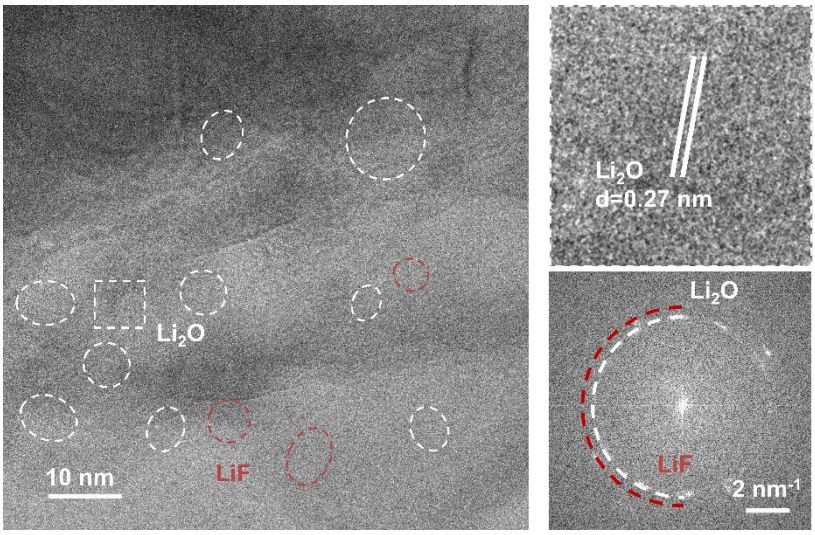

Figure S33 The HRTEM and corresponding FFT images of SEI cycled in electrolyte without HFA.

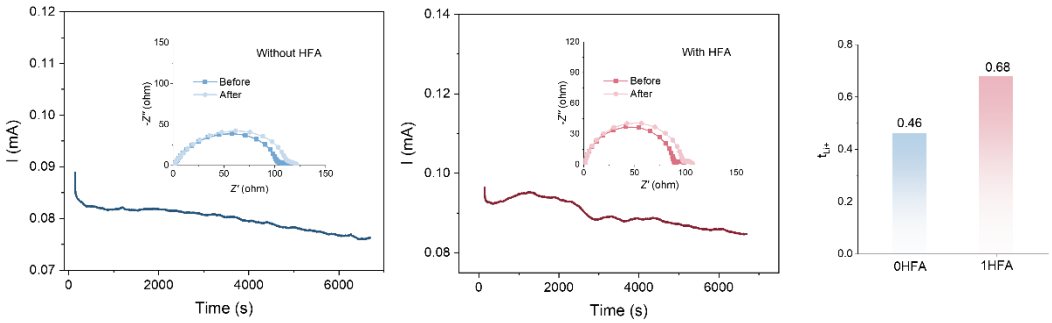

Figure S34 Comparison of t_{Li}^{+} of different electrolytes and the corresponding chronoamperometry profiles of Li||Li symmetric cells with different electrolyte.

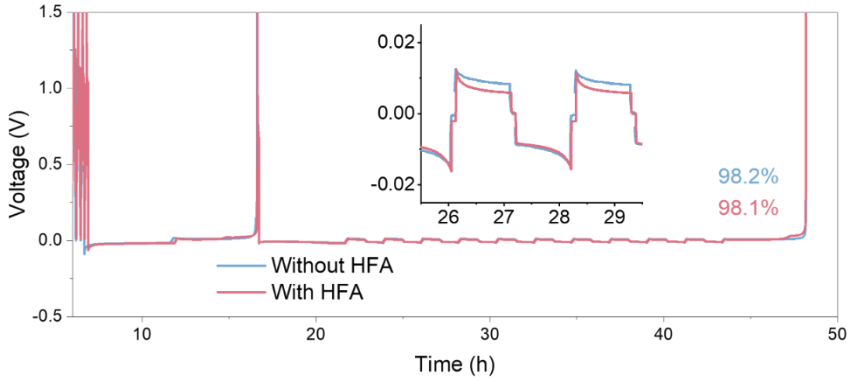

Figure S35 CE measurement by Aurbach's method.

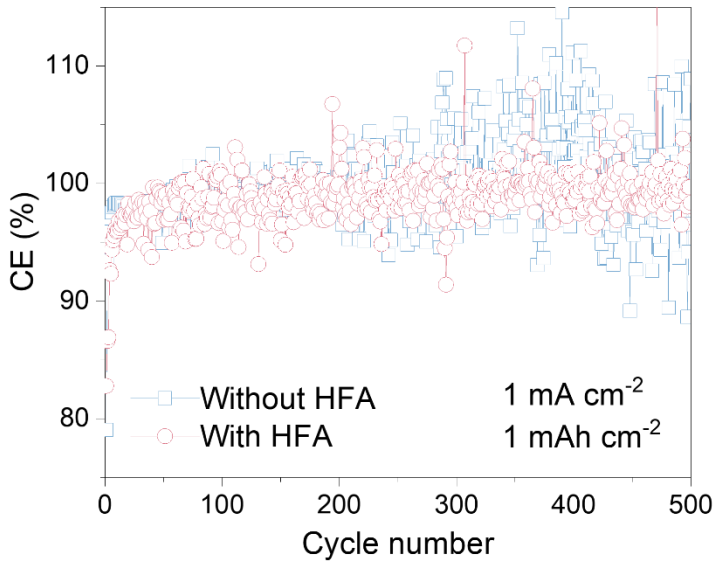

Figure S36 CE of Li||Cu cell using electrolyte with or without HFA addition at 1 mA cm^{-2} and 1 mAh cm^{-2}.

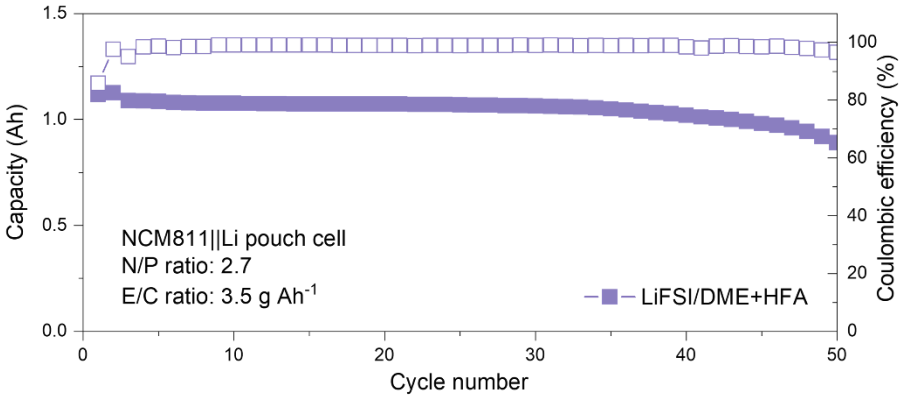

Figure S37 Cycling performance of 1Ah NCM811||Li pouch cell using designed electrolyte.

Table S1 Statistical results of anion-solvent number in first solvent sheath of Li^+ in LiFSI/DME electrolyte with or without HFA.

Without HFA		**With HFA**	
cluster	proportion	cluster	proportion
Li-3DME	**79.598%**	**Li-3DME**	**72.002%**
Li-2DME-1FSI	**19.863%**	**Li-2DME-1FSI**	**27.423%**
Li-2DME-2FSI	0.365%	Li-2DME-2FSI	0.447%
Li-1DME-2FSI	0.087%	Li-2DME	0.045%
Li-2DME	0.044%	Li-3DME-1FSI	0.040%
Li-3DME-1FSI	0.031%	**Li-2DME-1FSI-1HFA**	**0.026%**
Li-1DME-3FSI	0.013%	**Li-2DME-1HFA**	**0.016%**
		Li-1DME-2FSI	0.002%

Table S2 Comparison of our work with reported electrolyte investigation works on NCM||Li pouch cells.

Electrolyte	Cell condition (Voltage range)	Current density (Charge/Discharge)	Cycling condition and capacity retention
1.5 M LiFSI DME[13]	NCM811||Li (2.8-4.3 V)	/	~80% after 25 cycles
1.5 M LiFSI DMMS[13]	NCM811||Li (2.8-4.3 V)	/	~96% after 140 cycles
3.2F-0.8N-TTE[14]	NCM811||Li (2.8-4.3 V)	0.1 CC/0.1 CD	88% after 86 cycles
NGPE[15]	NCM811||Li (2.8-4.3 V)	0.5 CC/0.5 CD	~90% after 200 cycles
LiFSI-TTE/BTFE[16]	NCM811||Li (2.8-4.3 V)	0.1 CC/0.33 CD	~87% after 200 cycles
Hybrid-DOL/PDOL-TTE[17]	NCM622||Li (2.5-4.6 V)	0.15 CC/0.15 CD	~80% after 60 cycles
1 M LiFSI/DMTMSA[18]	NCM811||Li (3-4.7 V)	0.2 CC/0.5 CD	~80% after 100 cycles
1.8 M LiFSI/DPE[19]	NCM811||Li (2.5-4.3 V)	0.1 CC/0.33 CD	~78% after 150 cycles
This work (1.5 M LiFSI-TTE/DME+HFA)	NCM811||Li (3-4.5 V)	**0.2 CC/0.5 CD**	~90% after 150 cycles

Table S3 Cell parameters of the NCM811||Li pouch cell.

	Parameter	Value
NCM811 Cathode	Discharge capacity	200 mAh g^{-1}
	Loading	94.5%
	Area weight	16 mg cm^{-1}
	Area capacity	3.02 mAh cm^{-1}
	Number of layers	6
Al foil	Thickness	12 μm
Li anode	Specific capacity	3860 mAh g^{-1}
	Li thickness	40 μm
	Area capacity	~8 mAh cm^{-1}
	N/P ratio	2.7
Cu foil	Thickness	8 μm
Separator	Thickness	18 μm
Electrolyte	E/C ratio	3.5 g Ah^{-1}
Package foil	Thickness	115 μm
Pouch cell	Average voltage	3.8 V
	Capacity	1.2 Ah
	Total weight	0.0141kg
	Specific energy density*	323 Wh kg^{-1}

*Specific energy density = discharge energy (Wh) / total weight (kg). This is a more precise calculation method compared to the method: Specific energy density = discharge capacity (Ah) × mid-value voltage (V) / total weight (kg)

Table S4. Performance of high-energy-density Li metal batteries in this work and literature.

Energy density (Wh kg^{-1})	Cycle number	Capacity retention	Ref.
319	20	94%	20
380	86	93%	21
310	100	81%	22
300	100	88%	23
355	113	86%	24
260	120	95%	25
300	200	86%	16
414	70	99%	26
430	50	70%	27
340	60	90%	28
357	50	90.9	29
321	60	90%	30
420	50	84%	31
355	113	86%	32
325	100	80%	33
323	150	92.9%	This work

References:

1 T. H. Wan, M. Saccoccio, C. Chen and F. Ciucci, *Electrochimica Acta*, 2015, **184**, 483-499.

2 R. G. Parr and W. Yang, *(Oxford Univ. Press, Oxford, 1989)*.

3 P. J. Stephens, F. J. Devlin, C. F. Chabalowski and M. J. Frisch, *J. Phys. Chem.*, 1994, **98**, 11623–11627.

4 A. D. McLean and G. S. Chandler, *J. Chem. Phys.*, 1980, **72**, 5639–5648.

5 K. Raghavachari, J. S. Binkley, R. Seeger and J. A. Pople, *J. Chem. Phys.*, 1980, **72**, 650-654.

6 L. Martinez, R. Andrade, E. G. Birgin and J. M. Martinez, *J. Comput. Chem.*, 2009, **30**, 2157-2164.

7 W. L. Jorgensen and J. Tirado-Rives, *Proc. Natl. Acad. Sci.*, 2005, **102**, 6665−6670.

8 A. S. L. Gouveia, C. E. S. Bernardes, L. C. Tomé, E. I. Lozinskaya, Y. S. Vygodskii, A. S. Shaplov, J. N. C. Lopes and I. M. Marrucho, *Phys. Chem. Chem. Phys.*, 2017, **19**, 29617-29624.

9 M. J. Abraham, T. Murtola, R. Schulz, S. Páll, J. C. Smith, B. Hess and E. Lindahl, *SoftwareX*, 2015, **1-2**, 19-25.

10 G. Bussi, D. Donadio and M. Parrinello, *J. Chem. Phys.*, 2007, **126**, 014101.

11 J. D. Chai and M. Head-Gordon, *J. Chem. Phys.* , 2008, **128**, 084106.

12 Humphrey, D. W. and K. A. & Schulten, *J. Mol. Graph. Model.* , 1996, **14**, 33-38.

13 Y. Huang, R. Li, S. Weng, H. Zhang, C. Zhu, D. Lu, C. Sun, X. Huang, T. Deng, L. Fan, L. Chen, X. Wang and X. L. Fan, *Energy Environ. Sci.*, 2022, **15**, 4349-4361.

14 N. Sun, R. Li, Y. Zhao, H. Zhang, J. Chen, J. Xu, Z. Li, X. Fan, X. Yao and Z. Peng, *Adv. Energy Mater.*, 2022, **12**, 2200621.

15 Y. Meng, D. Zhou, R. Liu, Y. Tian, Y. Gao, Y. Wang, B. Sun, F. Kang, M. Armand, B. Li, G. Wang and D. Aurbach, *Nat. Energy*, 2023, **8**, 1023-1033.

16 C. Niu, H. Lee, S. Chen, Q. Li, J. Du, W. Xu, J.-G. Zhang, M. S. Whittingham, J. Xiao and J. Liu, *Nat. Energy*, 2019, **4**, 551-559.

17 X. Peng, T. Wang, B. Liu, Y. Li and T. Zhao, *Energy Environ. Sci.*, 2022, **15**, 5350-5361.

18 W. Xue, M. Huang, Y. Li, Y. G. Zhu, R. Gao, X. Xiao, W. Zhang, S. Li, G. Xu, Y. Yu, P. Li, J. Lopez, D. Yu, Y. Dong, W. Fan, Z. Shi, R. Xiong, C.-J. Sun, I. Hwang, W.-K. Lee, Y. Shao-Horn, J. A. Johnson and J. Li, *Nat. Energy*, 2021, **6**, 495-505.

19 Z. Li, H. Rao, R. Atwi, B. M. Sivakumar, B. Gwalani, S. Gray, K. S. Han, T. A. Everett, T. A. Ajantiwalay, V. Murugesan, N. N. Rajput and V. G. Pol, *Nat. Commun.*, 2023, **14**, 868.

20 L. P. Hou, N. Yao, J. Xie, P. Shi, S. Y. Sun, C. B. Jin, C. M. Chen, Q. B. Liu, B. Q. Li, X. Q. Zhang and Q. Zhang, *Angew. Chem. Int. Ed.*, 2022, **61**, e202201406.

21 Y.-H. Tan, G.-X. Lu, J.-H. Zheng, F. Zhou, M. Chen, T. Ma, L.-L. Lu, Y.-H. Song, Y. Guan, J. Wang, Z. Liang, W.-S. Xu, Y. Zhang, X. Y. Tao and H.-B. Yao, *Adv. Mater.*, 2021, **33**, 2102134.

22 Y. Xia, P. Zhou, X. Kong, J. Tian, W. Zhang, S. Yan, W.-h. Hou, H.-Y. Zhou, H. Dong, X. Chen, P. Wang, Z. Xu, L. Wan, B. Wang and K. Liu, *Nat. Energy*, 2023, **8**, 934-945.

23 Q. Zhao, N. W. Utomo, A. L. Kocen, S. Jin, Y. Deng, V. X. Zhu, S. Moganty, G. W.

Coates and L. A. Archer, *Angew. Chem. Int. Ed.*, 2022, **61**, e202116214.
24 P. Shi, Z.-H. Fu, M.-Y. Zhou, X. Chen, N. Yao, L.-P. Hou, C.-Z. Zhao, B.-Q. Li, J.-Q. Huang, X.-Q. Zhang and Q. Zhang, *Sci. Adv.*, 2022, **8**, eabq3445.
25 M. S. Kim, J.-H. Ryu, Deepika, Y. R. Lim, I. W. Nah, K.-R. Lee, L. A. Archer and W. I. Cho, *Nat. Energy*, 2018, **3**, 889-898.
26 P. Zhao, Y. Li, S. Chen, H. Fan, Y. Feng, L. Hu, Y. Zhang, Q. Nie, H. Pei, C. Yang, J. Deng, C. Bao and J. Song, *Adv. Energy Mater.*, 2022, **12**, 2200568.
27 W. Deng, W. Dai, X. Zhou, Q. Han, W. Fang, N. Dong, B. He and Z. Liu, *ACS Energy Lett.*, 2020, **6**, 115-123.
28 X. Q. Zhang, T. Li, B. Q. Li, R. Zhang, P. Shi, C. Yan, J. Q. Huang and Q. Zhang, *Angew. Chem. Int. Ed.*, 2020, **59**, 3252-3257.
29 K. Huang, S. Bi, B. Kurt, C. Xu, L. Wu, Z. Li, G. Feng and X. Zhang, *Angew. Chem. Int. Ed.*, 2021, **60**, 19232-19240.
30 J.-H. Kim, J.-M. Kim, S.-K. Cho, N.-Y. Kim and S.-Y. Lee, *Nat. Commun.*, 2022, **13**, 254.
31 L. Lin, L. Suo, Y. Hu, H. Li, X. Huang and L. Chen, *Adv. Energy Mater.*, 2021, **11**, 2003709.
32 Z. Chang, H. Yang, A. Pan, P. He and H. Zhou, *Nat. Commun.*, 2022, **13**, 6788.
33 Z. Yu, H. Wang, X. Kong, W. Huang, Y. Tsao, D. G. Mackanic, K. Wang, X. Wang, W. Huang, S. Choudhury, Y. Zheng, C. V. Amanchukwu, S. T. Hung, Y. Ma, E. G. Lomeli, J. Qin, Y. Cui and Z. Bao, *Nat. Energy*, 2020, **5**, 526-533.